PHYSICAL REVIEW APPLIED **9,** 054001 (2018)

Band-Gap Engineering in ZnO Thin Films: A Combined Experimental and Theoretical Study

Vani Pawar,[1] Pardeep K. Jha,[1,*] S. K. Panda,[2] Priyanka A. Jha,[1] and Prabhakar Singh[1]
[1]*Department of Physics, Indian Institute of Technology (Banaras Hindu University) Varanasi,*
Varanasi 221005, India
[2]*Centre de Physique Théorique, Ecole Polytechnique, CNRS UMR 7644,*
Université Paris–Saclay, 91128 Palaiseau, France

(Received 5 October 2017; revised manuscript received 27 February 2018; published 2 May 2018)

Zinc oxide thin films are synthesized and characterized using x-ray diffraction, field-emission scanning electron microscopy, atomic force microscopy, and optical spectroscopy. Our results reveal that the structural, morphological, and optical properties are closely related to the stress of the sample provided that the texture of the film remains the same. The anomalous results are obtained once the texture is altered to a different orientation. We support this experimental observation by carrying out first-principles hybrid functional calculations for two different orientations of the sample and show that the effect of quantum confinement is much stronger for the (100) surface than the (001) surface of ZnO. Furthermore, our calculations provide a route to enhance the band gap of ZnO by more than 50% compared to the bulk band gap, opening up possibilities for wide-range industrial applications.

DOI: 10.1103/PhysRevApplied.9.054001

I. INTRODUCTION

ZnO, being a direct wide-band-gap (3.2-eV) [1] semiconductor with a high exciton binding energy (60 meV) [2] at room temperature, has gained substantial attention in the last few decades due to its prospects for electronic and optoelectronic applications such as ultraviolet (UV) lasers, light-emitting diodes, and solar cells [3–6]. To exploit this material for a large number of optoelectronic applications, tailoring the size of the band gap is an important prerequisite. In particular, it is desirable to enhance the band gap to the highly blind region from 4.40 to 5.65 eV (220–280 nm) in order to make ZnO-based solar-blind photodetectors which have broad applications in chemical threat detection, flame sensing, and ultraviolet environmental monitoring [7–9].

A vast number of experimental [8,10–12] and theoretical [13,14] works have been devoted to finding routes to enhance the band gap of ZnO to make it suitable for a wide range of applications. Most of these studies [8,11,12,14] show that alloying with high-band-gap materials like MgO and BeO enable a widening of the band gap. Schmidt-Grund *et al.* [15] reported an increase of the band gap to 4.05 eV in $Mg_xZn_{1-x}O$ at 34% Mg concentration, compared to a band gap of 3.2 eV for pure ZnO [1]. (Be,Zn)O-based alloys were also initially thought to be great potential materials for wide-band-gap engineering (up to 10.6 eV) [12]. However, later studies [11,16] confirmed its incompetency for band-gap engineering due to the large lattice mismatch between BeO and ZnO. Moreover, BeO is a fragile toxic material and thus is not a good candidate for large-scale applications. Therefore, we need to explore other means to extend the band gap of ZnO to a considerably large value in the UV region.

A dimensional reduction from bulk to surface is considered to be another important route for widening the band gap and tuning the electronic properties. Thickness-dependent electronic properties of transition-metal surfaces have emerged as an important field of research in recent years [17–20]. Mak *et al.* [18] reported a confined induced shift in the indirect band gap of MoS_2 from a bulk value of 1.3–1.9 eV in the monolayer limit. A similar trend of band-gap enhancement has also been found for hexagonal boron nitride and for a few transition-metal dichalcogenides [17,19]. Although there is a vast amount of literature on the bulk and surface electronic properties of ZnO, very little is known about the thickness and texture dependence of the surface electronic and optical properties.

In view of the above, we prepare the ZnO thin films using the sol-gel technique and study its optical properties for various thicknesses. Our main focus during the synthesis is to minimize the effect of extrinsic factors such as processing parameters and impurities so that the intrinsic behavior of ZnO thin films can be understood. We employ a number of experimental techniques, such as x-ray diffraction, field-emission scanning electron microscopy (FESEM), atomic force microscopy (AFM), and optical spectroscopy to understand the structural and morphological concerns and their relation to the optical properties. Furthermore, to provide a detailed microscopic understanding of our experimental results and to analyze the quantum confinement effects on various ZnO surfaces, we present hybrid functional

---

[*] pardeepjha.jiit@gmail.com, pardeepk.pf.phy17@iitbhu.ac.in

© 2018 American Physical Society

calculations which provide a very precise estimation of the band gap. Our theoretical results find stronger quantum confinement effects on the (100) surface than the (001) surface of ZnO. We report that a widening of the band gap up to the blind region (above 4.4 eV) is possible only by reducing the number of bilayers in a ZnO thin film, opening up an alternative route for additional industrial applications. Our theoretical study attempts not only attempts to understand the experimental results of this paper but also aims to motivate further experimental activities in this area, especially in terms of the synthesis of ZnO thin films with very small thicknesses.

II. EXPERIMENTAL AND THEORETICAL METHODS

A. Sample preparation and measurements

ZnO thin films have been fabricated by several techniques in the past [21–27]. Among these techniques, the sol-gel method offers a promising processing route due to a number of advantages in comparison to other deposition methods. Some of the advantages include the excellent control of stoichiometry, the low cost, and the simple, safe, and easy doping in film composition [27]. Thus, in this investigation, ZnO thin films are synthesized by the sol-gel technique on a glass substrate. Zinc acetate dihydrate [ZAD: $Zn(CH_3COO)_2 \cdot 2H_2O$], ethanol ($C_2H_5OH$), and monoethanolamine (MEA: $H_2NCH_2CH_2OH$) are used as a precursor, a solvent, and a stabilizer material, respectively. ZAD is dissolved in a mixture of ethanol with a molar concentration of $0.75M$ and a MEA solution added to this mixture drop by drop. The resultant solution is stirred at 60 °C for 120 min. It yields a clear and homogeneous solution for the deposition. The freshly prepared solution is spin coated on the glass substrate. The glass substrates are cleaned ultrasonically with HNO_3, deionized water, ethanol, and acetone, respectively, for 10 min each. The substrates are preheated at 250 °C for 5 min before taking the deposition. The thin films are fabricated on a glass substrate using a spin-coating unit, rotated at 3000 rpm for 60 s followed by a heating at 250 °C for 5 min to evaporate the extra solvent and organic residuals. The multilayer thin films are obtained by following the same procedure, simply by repeating the same process N times for N multilayers. The films are then annealed in air at 500 °C for 1 h and cooled down up to the ambient temperature in order to obtain the crystallized ZnO, as illustrated in Fig. 1(a). The thin film prepared is hereafter abbreviated as Z_N ($N = 1$, 2, 3, and 4, where N indicates the number of ZnO layers). The thicknesses of these thin films are measured using the SemiconSoft MProbe series thin-film measurement system, and they are found to be approximately 43, 110, 113, and 115 nm. We call these samples Z_1, Z_2, Z_3, and Z_4, respectively, in the rest of the article.

Surface morphologies are investigated by FESEM and AFM and are shown in Figs. 1(b) and 1(c), respectively. The FESEM micrographs exhibit a fiberlike network structure in all of the samples which is distributed over the complete surface of the film, indicating polycrystalline crystal growth. The same fiberlike network is also confirmed at the atomic level, as observed in our AFM images [see Fig. 1(c)].

To determine the phases, ZnO thin films are characterized by an x-ray diffraction (XRD) technique using Rigaku MiniFlex. The obtained XRD pattern is displayed in Fig 1(d). It shows a polycrystalline phase with three strongest peaks that can be indexed with (002), (100), and (101). The pattern is matched with a Joint Committee for Powder Diffraction Standards (JCPDS) card (No. 36-1451) and confirms the formation of a hexagonal wurtzite structure with space group $P6_3mc$.

Optical absorption is obtained using a PerkinElmer LAMBDA 750 UV/Vis spectrophotometer, and the obtained spectrum is shown in Fig. 1(e). The absorption edges are found to be at about 388, 390, 394, and 404 nm, respectively. The observations are further verified since the films are transparent when seen in UV light with a shorter wavelength (UV-C), while it appears black under UV light with a longer wavelength (UV-A) [see the inset of Fig. 1(e)].

B. Computational details

The calculations are carried out using the projector-augmented-wave method [28,29] as implemented in the Vienna *ab initio* simulation package (VASP) [30,31]. Three different functionals—the generalized-gradient approximation (GGA) functional of Perdew, Burke, and Ernzerhof (PBE) [32], GGA + U [33] (the Hubbard U), and the PBE0 hybrid functional [34,35]—are employed to understand and analyze our experimental results. The GGA functional is primarily used only for the ionic relaxation in which their positions are relaxed to minimize the Hellmann-Feynman force on each atom with a tolerance value of 0.01 eV/Å. To analyze the on-site electron-electron correlation effects, the GGA + U method [33] is employed while considering $U = 8$ eV and Hund $J = 0.9$ eV. These interaction parameters are taken from the constrained random-phase approximation calculations of Ref. [36]. We see below that, among these functionals, the hybrid functional PBE0 provides the most accurate description of the electronic properties of bulk ZnO. Thus, in order to provide a reliable description of the surface properties, all of the surface calculations are carried out employing the PBE0 hybrid functional [35]. The kinetic-energy cutoff for the plane-wave basis is chosen to be 600 eV and a $10 \times 10 \times 6$ k mesh is used for Brillouin-zone integration in all of the bulk calculations.

Two surface structures, (001) and (100), are simulated using the symmetric slab model for the calculated equilibrium geometry. These slabs are finite in the z direction but periodic in the x and y directions, and we use a 16-Å vacuum region to confine the system along the z direction. Ionic relaxation of the upper three layers is performed, while the rest are fixed to bulk positions. The residual internal electric field in these thin slabs is quenched by saturating the broken

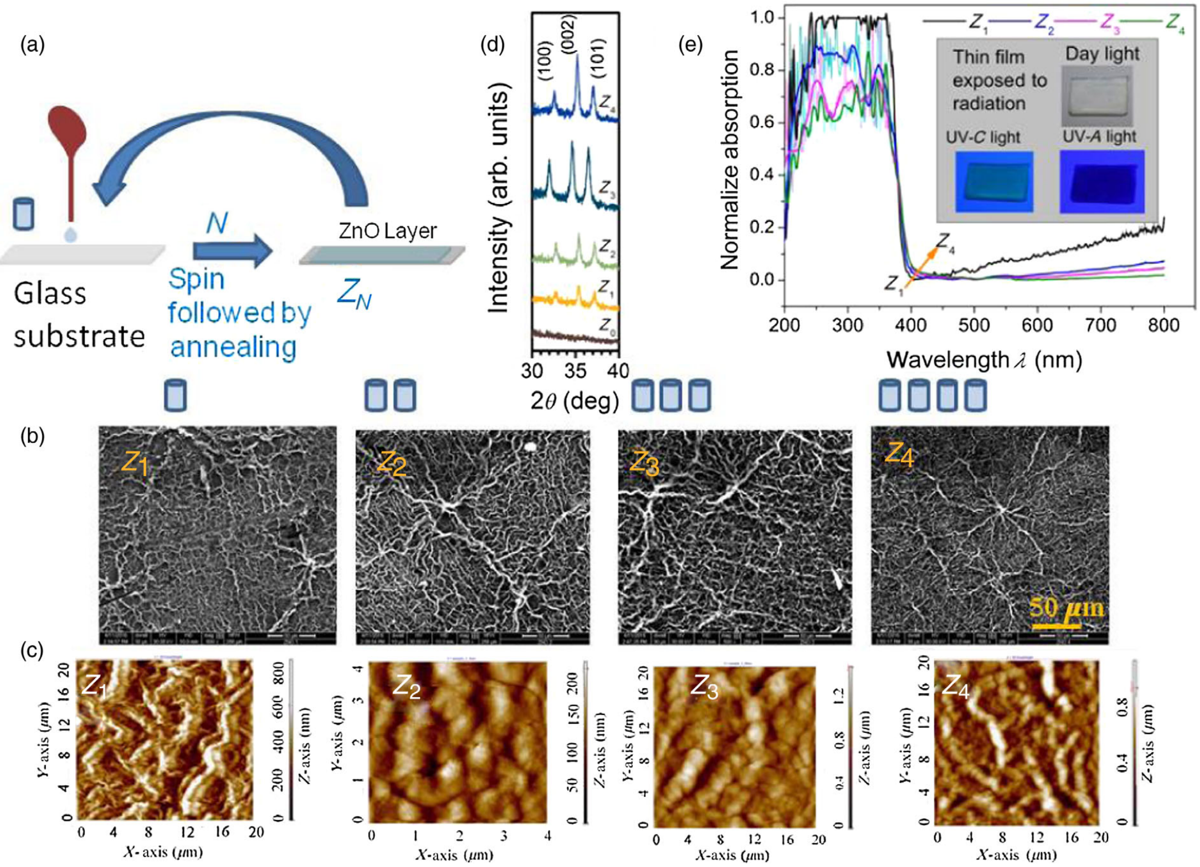

FIG. 1. (a) A schematic diagram of the layer deposition of ZnO thin films by a spin-coating unit, abbreviated as Z_N ($N = 1, 2, 3$, and 4, where N indicates the number of ZnO layers). Z_0 represents the glass substrate. (b) FESEM and (c) AFM micrographs. (d) The x-ray diffraction pattern of the thin films. (e) The normalized optical absorption spectrum. (Inset) Images of the thin films when the are exposed to daylight, UV light with a shorter wavelength (UV-*C*) in the range of 100–280 nm, and UV light with a longer wavelength (UV-*A*) in the range of 315–400 nm.

surface bonds on both sides with hydrogenlike atoms. An artificial atom with a nuclear charge of 1/2 and 3/2, respectively, is added for each O and Zn surface atom to guarantee that the surface bands are always fully occupied and that the ideal charge neutralization for the sides of the slabs is enforced. Furthermore, for the (001) surface, we use a $8 \times 8 \times 1$ k mesh, while, for the 100 surface, a $8 \times 6 \times 1$ k mesh is considered.

The stability of the surface structures corresponding to the lowest thicknesses is checked by calculating the phonon frequencies at the Γ point of the Brillouin zone using density-functional perturbation theory (DFPT) [37]. The absence of any imaginary frequency mode for both of the surface structures, as discussed in the Appendix, establishes the stability of the system.

III. EXPERIMENTAL RESULTS AND DISCUSSION

A. Microstructural studies

Figure 1(b) shows the fiberlike network on the film surface. With layer deposition, the densification in the network is observed in the FESEM images. However, a dark background also appears. Thus, these results demonstrate that our samples consist of a fiber network and a background. We refer to the fiber phase as case 1 and the background as case 2 in the rest of the article. It is known that lesser thermal treatment to thin films leads to an amorphous phase. In order to inspect this, we try to find first the amorphicity present in the sample (if there is any), then the stoichiometry in both the fiber and the background.

The XRD pattern at a lower angle reveals the amorphous nature of a glass substrate. Figure 2(a) shows a broad XRD pattern (processed) for a glass substrate between 10° and 30°, with a peak at about 20° on a 2θ scale. It is further followed by the crystalline phase of ZnO, which we discuss while describing Fig. 1(d). The XRD patterns do not show a horizontal base, and they are not parallel for different layers. Furthermore, the FESEM image is analyzed to give the surface morphologies a bare glass surface (the white spot), as seen in Fig. 2(b) for two extreme thin-film samples, Z_1 and Z_4. Better crystallinity is observed with layer deposition at both locations for cases 1 and 2, as revealed in Fig. 2(c). In this figure, broadness appears in the (100) peak of Z_1. In the case of Z_4, the peak is much

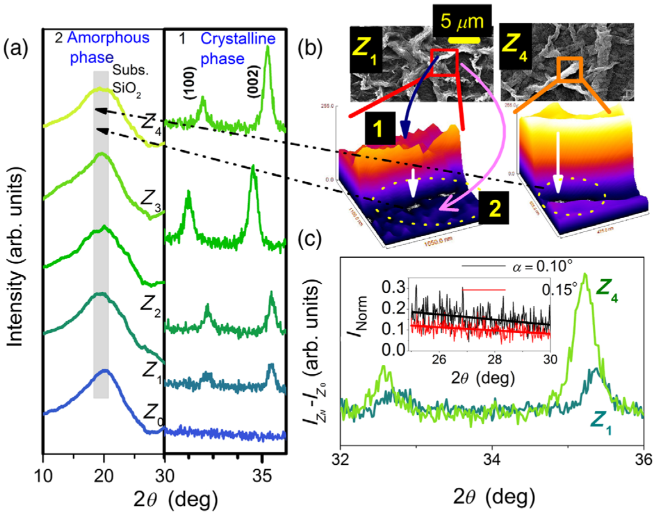

FIG. 2. (a) XRD pattern of thin films (Z_1–Z_4) including a glass substrate (Z_0). The presented data are smoothed for $10° \leq 2\theta \leq 30°$ to show the broadness and the peak of an amorphous glass substrate, while they are unprocessed for $2\theta > 30°$, revealing the crystalline nature of ZnO. (b) The magnified FESEM image and the corresponding surface plots of thin films Z_1 and Z_4, revealing the difference between the very crystalline fiber (case 1) and the partial amorphous bedding in the background (case 2). (c) A comparative XRD pattern of Z_1 and Z_4 (with Z_0 subtracted) showing that the presence of amorphicity in thin films reduces upon an increase in layers. (Inset) The XRD background of the Z_4 sample for two different glancing angles, $\alpha = 0.10°$ and 0.15°.

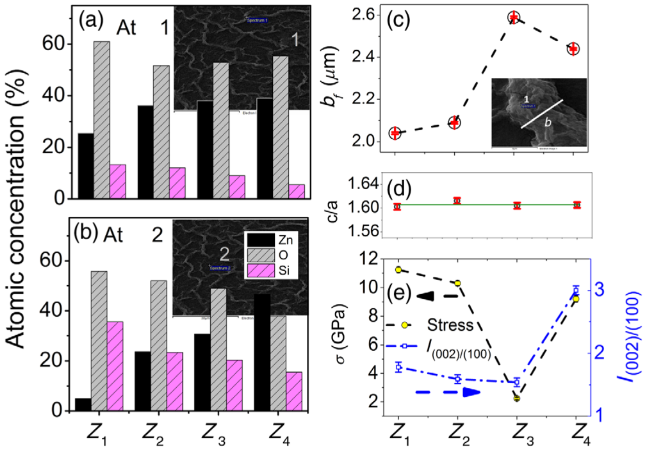

FIG. 3. Atomic percentage of Zn, O, and glass (Si) on (a) the nanofiber (case 1; the SEM image is shown in the inset) and on (b) the background (case 2; the SEM image is shown in the inset) as obtained from energy-dispersive x-ray analysis measurements. (c) The average fiber widths, (d) tetragonality (c/a), (e) the in-plane stress and texture along the c axis (I_{002}/I_{100}) of the four samples. The inset of (c) shows the SEM image of the fiber width for case 1. The respective error bars are shown in red.

sharper and a large growth in the crystalline phase appears. With the change of the glancing angle from $\alpha = 0.10°$ to 0.15°, the background of the XRD pattern does not match, and the XRD patterns are not horizontal [see the inset of Fig. 2(c)], indicating the presence of partial amorphicity in case 2, i.e., the background.

The stoichiometry of a film investigated using the energy-dispersive x-ray (EDX) spectrum is shown in Figs. 3(a) and 3(b). The EDX measurements are carried out on the nanofiber [case 1, Fig. 3(a)], and also on the background portion [case 2, Fig. 3(b)]. The measurements reveal the atomic percentage of the elemental compositions that exists in the ZnO thin films. The well-defined peak corresponding to Zn and O confirms that the constituent elements are present in the sample. It is revealed from the EDX analysis that the fiber network is composed of ZnO. It is noticed that, upon increasing the layers of ZnO film, the elemental atomic percentage distribution of Zn in case 1 gradually increases in samples Z_1, Z_2, and Z_3, while there is a slight decrease in Z_4. On the other hand, in case 2, there is a continuous increase in the atomic percentage of Zn. A careful comparative observation of the data indicates that, up to Z_3, the fiber amassment is more; thereafter, it saturates and shifts to the interior. Thus, in case 2, the concentration of Zn increases gradually as we move from Z_1 to Z_4 and becomes approximately 40%, which is almost equal to the concentration in case 1. This observation confirms the presence of ZnO in the fiber and background portions.

Furthermore, to understand more about the fibers, we calculate the average width of the fiber (b_f) using the FESEM micrograph. As shown in Fig. 3(c), it is observed that the b_f value increases up to sample Z_3, and there is a slight decrease for Z_4. The similar nature of the increase and the decrease is observed also in the atomic distribution of Zn for the fiber (i.e., case 1). However, in case 2, an increasing trend in the concentration of Zn is observed. From these results, we conclude that the materials are a composite of crystalline fiber and an amorphous background of ZnO and thus that case 1 is a crystalline fiber and case 2 is an amorphous background. Because of the concentration difference of Zn in the two cases, there would be intrinsic stress in the thin films, as presented in Fig. 3(e). The stress is found to reduce to a very low value as we go from Z_1 to Z_3 but, surprisingly, to increase for the Z_4 sample. Furthermore, it is observed that, up to Z_3, the width parameter is directly related to the number of layers of thin films, but it decreases for Z_4.

The comparative analysis of the XRD patterns of these four thin films reveals that, up to Z_3, all major peaks shift towards the lower-angle side; thereafter, a sudden shift towards a higher angle is observed for Z_4 [see Fig. 1(d)]. Knowing the interplanar spacing, i.e., the d value from Bragg's law, the lattice parameters a and c are obtained using the formula for a hexagonal system:

$$\frac{1}{d_{hkl}^2} = \frac{4(h^2 + hk + k^2)}{3a^2} + \frac{l^2}{c^2}, \tag{1}$$

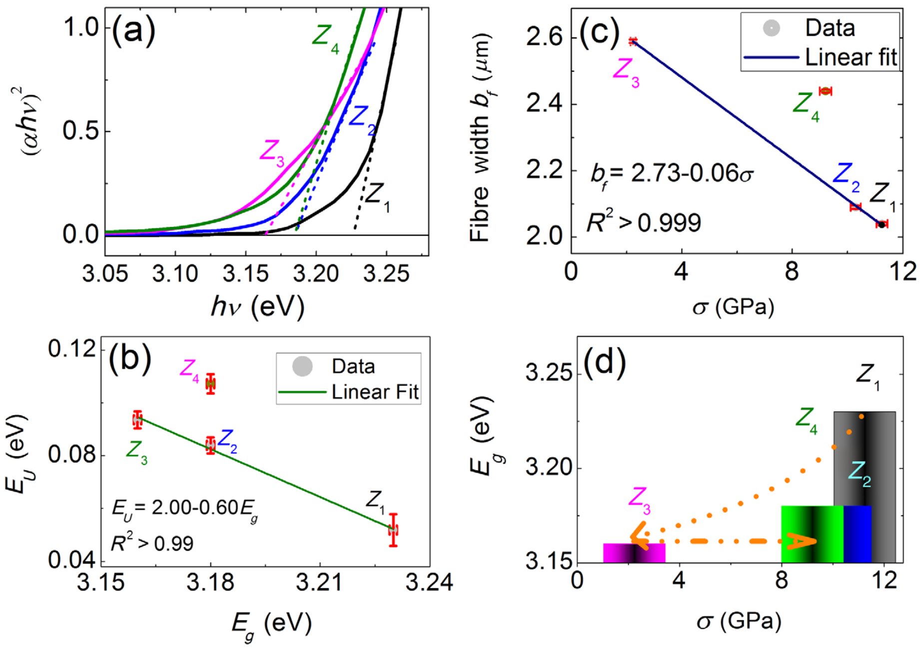

FIG. 4. (a) Variation of $(\alpha h\nu)^2$ as a function of the photon energy. (b) Urbach energy vs the band-gap plot. (c) The fiber width and (d) the band gap as a function of the in-plane stress along the c axis. The error bars are shown in red.

where, h, k, and l are Miller indices. The lattice parameter is calculated. It is evident that the lattice parameters c and a are almost constant in the layers, and hence the tetragonal strain, i.e., c/a [about 1.60; see Fig. 3(d)] is also constant. Furthermore, the crystallite size is estimated using the Debye-Scherrer formula using broadening of XRD peaks (002) and it is found be approximately 23, 20, 18, and 20 nm for Z_1, Z_2, Z_3, and Z_4, respectively. No particular trend is observed, nor is a significant variation in the crystallite size observed. What is important to observe here is the variation in intensity of the samples. We calculate the ratio of intensity of the (002) plane to the (100) plane, and it is found to be 1.78, 1.59, 1.54, and 3.00 for Z_1, Z_2, Z_3, and Z_4, respectively [Fig. 3(e)]. These findings clearly indicate that the Z_4 film has a better c-directional orientation (texture).

The stress in these thin films should not be extrinsic, as the difference in thermal expansion coefficient between glass and ZnO is too small to be significant. Thus, it must be intrinsic, which, in turn, depends on the defects and lattice distortions present in the sample [38]. The stress (σ) in the plane can be obtained by using the biaxial strain model [39]:

$$\sigma = \left[2C_{13} - \frac{C_{11} + C_{12}}{C_{13}} C_{33}\right] \frac{(d - d_0)}{d_0}, \qquad (2)$$

where C_{ij} represents the elastic stiffness constants, d and d_0 are the interplanar spacings corresponding to the (002) plane and the unstrained system of ZnO thin films (2.603 Å, per JCPDS Card No. 36-1451), respectively. The values of these stiffness constants are reported to be $C_{11} = 209.7$, $C_{12} = 121.1$, $C_{13} = 105.1$, and $C_{33} = 210.9$ GPa [39]. The calculated values of σ for different samples are plotted and shown in Fig. 3(e). The positive values of stress reveal the tensile nature of stress in these thin films. As we predicted earlier, stress is reduced in the layers of ZnO and becomes lowest for Z_3, while it is found to increase again for the Z_4 sample, which may be attributed to the reduction of the width parameter of the sample.

B. Optical properties

The energy band gap (E_g) in the case of a wideband transparent conducting oxide is related to stress. Stress in the crystal may change the electronic structure of the materials, and hence there may be band-gap tuning. The energy band gap depends on the crystallite size but, in the present case, no significant variation in crystallite size is observed, as it is 25 ± 3 nm in all of the films. So, in this particular case, we are able to keep various factors, like annealing temperature, substrate, etc., at a practically constant value. As we select pure ZnO, the stress in the sample is due only to the concentration of the precursor and repeated processing. Hence, the stress generated in the films must be intrinsic in nature.

In order to find the band gap, it is necessary to verify which transmission mode is applicable to these films. For this purpose, the $(\alpha h\nu) = A(h\nu - E_g)^n$ relation is used, where A is the absorption-edge width parameter, h is Planck's constant, E_g is the optical direct band-gap energy, ν is the frequency of incident radiation, and the value of n determines whether the transmission mode is allowed or forbidden. It is found that the values of n are 0.56 (Z_1), 0.66 (Z_2), 0.66 (Z_3), and, for Z_4, an ideal 0.5, which is referred to as the direct and allowed transition. Thus, the band-gap value is estimated using the Tauc relation, i.e., $(\alpha h\nu) = A(h\nu - E_g)^{1/2}$ [Fig. 4(a)] and the energy gap is found to be

3.23, 3.18, 3.16, and 3.18 eV, respectively. This increase in band gap for the Z_4 sample is further tested by an estimation of the energy tail width, E_U [the Urbach rule, $\alpha = \alpha_0 \exp(h\nu/E_U)$]. Similar to most of the materials [40], a linear relation between E_U and E_g is found up to Z_3, as shown in Fig. 4(b).

In order to find the correlation between stress, energy gap, and the width parameter, Figs. 4(c) and 4(d) are plotted. It is observed that the width parameter and tensile stress present in the sample nicely show a linear behavior for three samples, namely, Z_1, Z_2, and Z_3. However, the data corresponding to Z_4 do not obey this linear relation [Fig. 4(c)]. The energy gap as a function of stress does not follow the expected linear relationship even for the first three samples. This result is highly surprising as, till now (to the best of our knowledge), the reported literature has indicated that the relationship should be linear. The unusual behavior of Z_4 with respect to all three relations [Figs. 4(b)–4(d)] is more surprising since structural, morphological, and optical properties are expected to behave uniformly.

Although the results are both different (the stress–fiber width relation) and anomalous (the nonlinear stress–band gap relation), Z_4 does not fit with any of these relations, even in an obvious band gap–Urbach energy relation, as is clear in Figs. 3 and 4. Experimentally, the only difference that we could confirm from other thin films is the texture change (from about 1.5 to 3.0) in Z_4. Hence, it is concluded that Z_4 has a more c-directional orientation.

In order to better understand our experimental results—particularly the dependence of the band gap on the orientation of the sample—and also to provide various routes to tune the band gap of ZnO, we investigate the electronic structure of wurtzite ZnO and its surfaces using the first-principles calculations.

IV. THEORETICAL RESULTS AND DISCUSSION

A. Optimized lattice parameters and band gap of bulk ZnO

The wurtzite phase of ZnO is characterized by three parameters: the lattice constants a and c and the internal parameter u, which is the z coordinate of the O ion. To begin with, we perform a full structural optimization of both the lattice parameters and the internal coordinates using three different functionals, as mentioned above. The results of our calculations are summarized in Table I. We observe that a pure GGA functional such as PBE overestimates a and c by 0.5% and 3.1%, respectively. These findings agree quite well with the previous reports [41,42]. This result is expected since the density-functional theory within the local-density approximation (LDA)—as well as its semilocal extension, the GGA—underestimates the binding energy of localized d states due to an incomplete cancellation of the artificial Hartree self-interaction term. As a consequence, these methods overestimate the hybridization between the Zn $3d$ electrons and the O $2p$ valence electrons, resulting in a poor description of the crystal geometry and of other properties such as the band gap which are discussed later. To overcome the limitations of the LDA GGA, the common practice is to add an orbital-dependent Hubbard U–like term for the d states within the LDA and/or GGA+U framework [33]. Table I shows that the GGA + U approach slightly improves the results but still gives underestimations of 0.8% and 1.6% for a and c, respectively, over the experimental values. Hybrid functionals, which include part of the nonlocal Hartree-Fock–type exchange in the exchange-correlation functional, provide a much improved description of the binding energy and, consequently, the hybridization between the d and p states, resulting in the most accurate description of the properties of ZnO.

TABLE I. Structural parameters and band gap of bulk ZnO. Experimental values of the bulk lattice parameters are taken from Ref. [43].

Functional	a (Å)	c (Å)	u	Gap (eV)
GGA	3.27	5.36	0.3757	0.70
GGA + U	3.23	5.11	0.3839	1.72
Hybrid (PBE0)	3.26	5.21	0.3818	3.14
Experiment	3.25	5.21	0.3820	3.30

Thus, the best estimation of the lattice parameters is found when the hybrid functional PBE0 is employed (see Table I). The importance of using a hybrid functional becomes more evident when the band gap of bulk ZnO is compared using these methods. The band gaps obtained from the GGA and GGA + U are, respectively, 0.70 and 1.72 eV, which are highly underestimated in both of the methods. It is well known that not only are the band gaps underestimated by the GGA, but the positions of the energy levels of the Zn $3d$ electrons are overestimated, as discussed in Refs. [44,45]. The inaccurate determination of the order of states at the topmost valence band from the GGA and GGA + U approaches is also discussed in Refs. [44,46]. The calculated band gap using the hybrid functional comes out to 3.14 eV, which is very close to the experimental band gap of 3.30 eV [43] and 3.18 eV for the bulk sample (in the present case). We see below that the position of the Zn d states and the overall electronic structure are also best described by the hybrid functional technique. In view of that, although hybrid functional calculations with periodic boundary conditions are computationally demanding, we adopt this method to provide a very accurate description of the surface electronic structure of ZnO and to explain the anomaly observed in the width-dependent nature of the band gap. We will also analyze the routes to increase the band gap of ZnO surfaces.

B. Electronic structure of bulk ZnO and its (001) and (100) surfaces

The total density of states (DOS) and m_l projected DOS (PDOS) of bulk ZnO are displayed in Fig. 5(a). The results

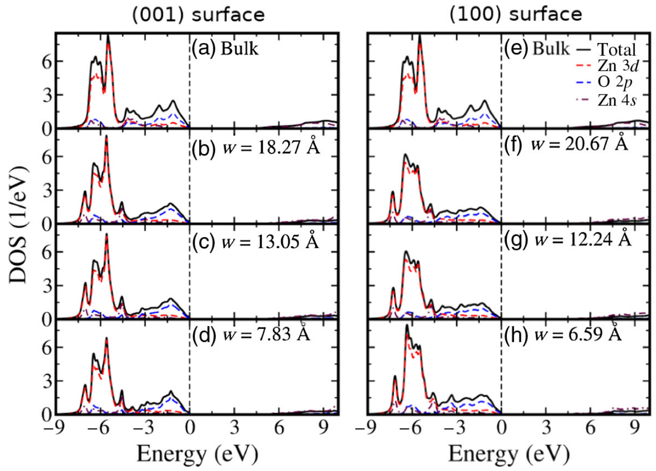

FIG. 5. Total and partial density of states for (a) bulk ZnO and its (001) polylayers of three different thicknesses (w): (b) 18.273 Å, (c) 13.052 Å, and (d) 7.831 Å. Similarly, (e) bulk ZnO and (100) polylayers of three different thicknesses, (f) 20.666 Å, (g) 12.245 Å, (h) 6.594 Å, are shown in the right-hand panels. For the partial density of states, only the projections of the top surface atoms are shown. The vertical dashed lines indicate the Fermi level.

show that bulk ZnO is an insulator with a gap of 3.14 eV. The partial densities of states of the Zn d, O p, and Zn s states reveal that the fundamental band gap arises due to the transition from the O $2p$–rich states at the top of the valence band to the bottom of the conduction band, where the states are predominantly of Zn $4s$ character. The overall valence-band spectra and the relative positions of the Zn d and O p states are in perfect agreement with the experimental spectra [47].

After providing a very reliable description of the bulk electronic structure, we now focus on the electronic properties of ZnO layered structures with respect to the slab thickness (w) of the system. Figure 5 shows the total DOS and PDOS of the (001) and (100) surfaces, respectively, going from bulk to a very thin layer. The shape, bandwidth, and position of the $3d$ states of a Zn ion on the (001) surface remain almost unaltered with a change in width of the sample. However, the position of the Zn $4s$ states in the conduction band make a blueshift, leading to an enhancement of the band gap as a function of decreasing slab thickness (see Fig. 5). Upon changing the surface orientation to (100), we observe two significant changes in the electronic structure: the shape of the Zn d states changes substantially and the band gap increases more rapidly with a decreasing slab thickness (see Fig. 5). These results are better visualized when the variations of the band gaps for both of the surfaces are plotted as a function of surface thickness, as displayed in Fig. 6. Our results demonstrate that the bulk band gap of the (001) surface is reached for thicknesses above 18 Å. With decreasing thickness, a progressive confinement-induced shift in the band gap from a bulk value of 3.14 to over 3.97 eV at a thickness of 7.83 Å is observed. This observation provides a route to tune the band gap of ZnO, which is extremely useful for technological applications. Interestingly, the rate of monotonic growth of a band gap with a decreasing slab thickness is found to be much stronger for the (100) surface. We observe that the band gap of the (100) surface grows from 3.49 eV at 20.67-Å thickness to 4.71 eV at a slab thickness of 6.59 Å. This observation implies that the confinement effect is stronger on the (100) surface than on its (001) counterpart. Therefore, our calculations reveal that the realization of a much wider gap insulator is possible in ZnO by simply changing the orientation of the surface, suggesting another route to tune the band gap of ZnO. In particular, the band gap would be extremely large in the monolayer limit, as evident from the slope of the (100) curve in Fig. 6. We note here that, due to the predictive power of the hybrid functional, our results provide not only the generic characteristics of the width dependence of the band gap for the (001) and (100) surfaces but also a quantitatively accurate estimation of the band gap.

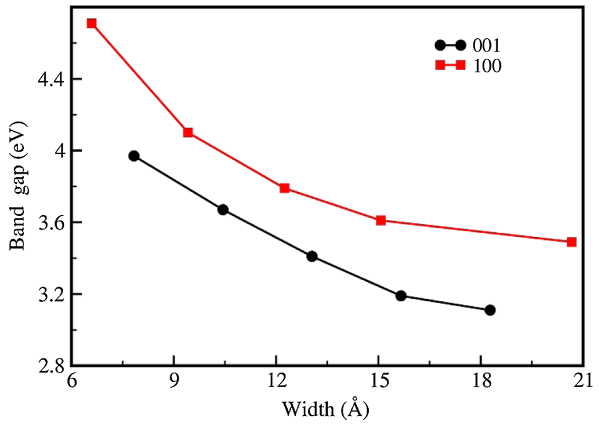

FIG. 6. The calculated band gap as a function of the thickness of the sample for the (001) and (100) surfaces.

Another key finding of our results is that, for every thickness, the band gap is higher for the (100) surface than the (001) surface (see Fig. 6). This characteristic feature of the surfaces is maintained even when the band gap reaches its saturated value at a large thickness of the sample. Since the experiments of this work are done for thin films with very large thicknesses, we will compare the experimental data with the theoretically calculated saturated values of the band gap. As pointed out before, our Z_4 sample has a different orientation than the other three samples (Z_1, Z_2, and Z_3), leading to a sudden increase in the band gap of the Z_4 sample. We also find that, for all of the samples, the theoretically estimated values of the band gaps are in good agreement with our experimental results.

V. CONCLUDING REMARKS

It is well known that the Burstein-Moss (BM) effect increases the band gap due to occupation of the lower edge of the conduction band, and therefore the Pauli exclusion rule does not allow the lower edge of the conduction band to be occupied [48,49]. In the present case, the band gap for bulk ZnO is found to be 3.18 eV. For the first layer, the band gap is observed to be 3.23 eV, so the BM effect for Z_1 can be effective. Accidentally, the difference between the band-gap energy of the Z_1 sample and the bulk sample is almost equal to the Urbach energy, i.e., approximately 50 meV. Upon further layering, there are reductions in stress, band gap, fiber width, and texture, and an increase in Urbach energy. These findings may be due to many-body interactions [50] which renormalize the energy states, and hence the nonlinear energy-stress relation is observed. Anomalous behavior appears in the Z_4 sample, as it is found that the tensile stress suddenly increases and the reduction in the fiber width hints at densification or orientational alteration along one particular direction. Furthermore, the Urbach tail energy (the quantum energy tail) is at maximum for this sample. In the present case, as mentioned earlier, the Z_4 sample is highly oriented in the c direction, as revealed by the experimental results. Theoretically, we are able to show that the change in texture can significantly influence the values of the band gaps. Thus, we can conclude that the optical band gap not only depends on the in-plane stress—it depends greatly on the texture of the sample. Finally, we theoretically discuss the dependency of the band gap on the thickness of the slab, which is an important issue for industrial applications. It is found that the magnitude of the confinement effect can be significantly large, resulting in the realization of a very large gap in the ZnO thin film.

In conclusion, we report in this paper that the structural dimension (the width of fiber) of the nanostructure in ZnO is closely related to the energy band gap, energy tail width, and intrinsic stress of the samples. Both the experimental and theoretical results confirm that the orientation and the thickness of ZnO thin films could alter the band gap to a large extent. Moreover, our theoretical results show that the band gap of ZnO thin films can be enhanced to the solar-blind region, i.e., > 4.6 eV. The theoretical predictions, based on state-of-the-art first-principles calculations, also provide motivation for further experimental activities on ZnO thin films.

ACKNOWLEDGMENTS

The authors are thankful to Professor S. B. Rai (Department of Physics, BHU–Varanasi) for providing the optical studies.

APPENDIX: PHONON FREQUENCIES OF THE SURFACE STRUCTURES

In this appendix, we report the results of our phonon calculations within the GGA functional in order to analyze the stability of the thinnest surface structure corresponding to the (001) and (100) surfaces. We adopt the DFPT [37] method as implemented in the VASP code to calculate the phonon frequencies at the Γ point of the Brillouin zone. This method is considered to be very efficient and accurate for calculating the phonon modes.

The calculated phonon frequencies are listed in Tables II and III for a (001) surface of 7.83-Å thickness and a (100)

TABLE II. Phonon mode frequencies (in cm^{-1}) at the Γ point of the Brillouin zone for a (001) surface with $w = 7.83$ Å.

Mode no.	1	2	3	4	5	6	7	8
Frequency	2267.8	1688.7	528.1	520.7	508.1	508.1	431.0	431.0
Mode no.	9	10	11	12	13	14	15	16
Frequency	398.5	398.5	381.5	381.5	377.0	320.8	320.8	219.2
Mode no.	17	18	19	20	21	22	23	24
Frequency	125.4	80.2	80.2	49.9	49.9	0.2	0.2	0.4

TABLE III. Phonon mode frequencies (in cm^{-1}) at the Γ point of the Brillouin zone for a (100) surface with $w = 6.59$ Å.

Mode no.	1	2	3	4	5	6	7	8
Frequency	2195.8	2192.4	1582.2	1568.4	606.6	595.2	548.4	542.3
Mode no.	9	10	11	12	13	14	15	16
Frequency	528.8	512.4	506.4	480.9	474.3	458.3	442.9	418.4
Mode no.	17	18	19	20	21	22	23	24
Frequency	413.2	404.1	363.4	349.1	344.5	339.6	338.1	334.0
Mode no.	25	26	27	28	29	30	31	32
Frequency	229.0	180.4	172.6	155.7	115.5	91.1	88.8	75.3
Mode no.	33	34	35	36	...	...	...	...
Frequency	65.2	0.2	0.3	0.4	...	...	...	...

surface of 6.59-Å thickness, respectively. It is seen that the frequencies of all of the modes for both of the surfaces have positive values. This observation suggests that the thinnest surface structures of the (001) and (100) surfaces considered in this paper are stable. Although synthesis of such a thin layer of ZnO has not yet been achieved, our phonon calculations reveal that freestanding ZnO thin layers are quite stable.

[1] D. C. Reynolds, D. C. Look, B. Jogai, C. W. Litton, G. Cantwell, and W. C. Harsch, Valence-band ordering in ZnO, Phys. Rev. B **60**, 2340 (1999).

[2] C. Klingshirn and H. Haug, Optical properties of highly excited direct gap semiconductors, Phys. Rep. **70**, 315 (1981).

[3] Atsushi Tsukazaki, Masashi Kubota, Akira Ohtomo, Takeyoshi Onuma, Keita Ohtani, Hideo Ohno, Shigefusa F. Chichibu, and Masashi Kawasaki, Blue light-emitting diode based on ZnO, Jpn. J. Appl. Phys. **44**, L643 (2005).

[4] Michael H. Huang, Samuel Mao, Henning Feick, Haoquan Yan, Yiying Wu, Hannes Kind, Eicke Weber, Richard Russo, and Peidong Yang, Room-temperature ultraviolet nanowire nanolasers, Science **292**, 1897 (2001).

[5] D. M. Bagnall, Y. F. Chen, Z. Zhu, T. Yao, S. Koyama, M. Y. Shen, and T. Goto, Optically pumped lasing of ZnO at room temperature, Appl. Phys. Lett. **70**, 2230 (1997).

[6] Toru Aoki, Yoshinori Hatanaka, and David C. Look, ZnO diode fabricated by excimer-laser doping, Appl. Phys. Lett. **76**, 3257 (2000).

[7] U. Ozgur, Ya. I. Alivov, C. Liu, A. Teke, M. A. Reshchikov, S. Doan, V. Avrutin, S.-J. Cho, and H. Morko, A comprehensive review of ZnO materials and devices, J. Appl. Phys. **98**, 041301 (2005).

[8] Longxing Su, Yuan Zhu, Quanlin Zhang, Mingming Chen, Xu Ji, Tianzhun Wu, Xuchun Gui, Bicai Pan, Rong Xiang, and Zikang Tang, Solar-blind wurtzite MgZnO alloy films stabilized by be doping, J. Phys. D **46**, 245103 (2013).

[9] Y. N. Hou, Z. X. Mei, H. L. Liang, D. Q. Ye, S. Liang, C. Z. Gu, and X. L. Du, Comparative study of n-MgZnO/p-Si ultraviolet-B photodetector performance with different device structures, Appl. Phys. Lett. **98**, 263501 (2011).

[10] Hsu-Cheng Hsu, Chun-Yi Wu, Hsin-Ming Cheng, and Wen-Feng Hsieh, Band gap engineering and stimulated emission of ZnMgO nanowires, Appl. Phys. Lett. **89**, 013101 (2006).

[11] Longxing Su, Yuan Zhu, Quanlin Zhang, Mingming Chen, Tianzhun Wu, Xuchun Gui, Bicai Pan, Rong Xiang, and Zikang Tang, Structure and optical properties of ternary alloy BeZnO and quaternary alloy BeMgZnO films growth by molecular beam epitaxy, Appl. Surf. Sci. **274**, 341 (2013).

[12] Y. R. Ryu, T. S. Lee, J. A. Lubguban, A. B. Corman, H. W. White, J. H. Leem, M. S. Han, Y. S. Park, C. J. Youn, and W. J. Kim, Wide-band gap oxide alloy: BeZnO, Appl. Phys. Lett. **88**, 052103 (2006).

[13] Chang-Youn Moon, Su-Huai Wei, Y. Z. Zhu, and G. D. Chen, Band-gap bowing coefficients in large size-mismatched II–VI alloys: First-principles calculations, Phys. Rev. B **74**, 233202 (2006).

[14] Longxing Su, Yuan Zhu, Dingyu Yong, Mingming Chen, Xu Ji, Yuquan Su, Xuchun Gui, Bicai Pan, Rong Xiang, and Zikang Tang, Wide range bandgap modulation based on ZnO-based alloys and fabrication of solar blind UV detectors with high rejection ratio, ACS Appl. Mater. Interfaces **6**, 14152 (2014).

[15] Rüdiger Schmidt-Grund, Anke Carstens, Bernd Rheinlnder, Daniel Spemann, Holger Hochmut, Gregor Zimmermann, Michael Lorenz, Marius Grundmann, Craig M. Herzinger, and Mathias Schubert, Refractive indices and band-gap properties of rocksalt $Mg_xZn_{1-x}O$ ($0.68 \le x \le 1$), J. Appl. Phys. **99**, 123701 (2006).

[16] Mingming Chen, Yuan Zhu, Longxing Su, Quanlin Zhang, Anqi Chen, Xu Ji, Rong Xiang, Xuchun Gui, Tianzhun Wu, Bicai Pan, and Zikang Tang, Formation behavior of $Be_xZn_{1-x}O$ alloys grown by plasma-assisted molecular beam epitaxy, Appl. Phys. Lett. **102**, 202103 (2013).

[17] A. Kuc, N. Zibouche, and T. Heine, Influence of quantum confinement on the electronic structure of the transition metal sulfide TS_2, Phys. Rev. B **83**, 245213 (2011).

[18] Kin Fai Mak, Changgu Lee, James Hone, Jie Shan, and Tony F. Heinz, Atomically Thin MoS_2: A New Direct-Gap Semiconductor, Phys. Rev. Lett. **105**, 136805 (2010).

[19] Joongoo Kang, Lijun Zhang, and Su-Huai Wei, A unified understanding of the thickness-dependent bandgap transition in hexagonal two-dimensional semiconductors, J. Phys. Chem. Lett. **7**, 597 (2016).

[20] Changgu Lee, Hugen Yan, Louis E. Brus, Tony F. Heinz, James Hone, and Sunmin Ryu, Anomalous lattice vibrations of single- and few-layer MoS_2, ACS Nano **4**, 2695 (2010).

[21] Y. Natsume, H. Sakata, T. Hirayama, and H. Yanagida, Low temperature conductivity of ZnO films prepared by chemical vapor deposition, J. Appl. Phys. **72**, 4203 (1992).

[22] V. Craciun, J. Elders, J. G. E. Gardeniers, and Ian W. Boyd, Characteristics of high quality ZnO thin films deposited by pulsed laser deposition, Appl. Phys. Lett. **65**, 2963 (1994).

[23] Bingqiang Cao, Weiping Cai, Yue Li, Fengqiang Sun, and Lide Zhang, Ultraviolet-light-emitting ZnO nanosheets prepared by a chemical bath deposition method, Nanotechnology **16**, 1734 (2005).

[24] Seung Hwangbo, Yun-Ji Lee, and Kyu-Seog Hwang, Photoluminescence of ZnO layer on commercial glass substrate prepared by sol-gel process, Ceram. Int. **34**, 1237 (2008).

[25] Li-Wen Lai and Ching-Ting Lee, Investigation of optical and electrical properties of ZnO thin films, Mater. Chem. Phys. **110**, 393 (2008).

[26] Jiaoxian Yu, Baibiao Huang, Xiaoyan Qin, Xiaoyang Zhang, Zeyan Wang, and Haixia Liu, Hydrothermal synthesis and characterization of ZnO films with different nanostructures, Appl. Surf. Sci. **257**, 5563 (2011).

[27] F. J. Serrao, K. M. Sandeep, and S. M. Dharmaprakash, Annealing-induced modifications in sol-gel spin-coated Ga: ZnO thin films, J. Sol-Gel Sci. Technol. **78**, 438 (2016).

[28] P. E. Blöchl, Projector augmented-wave method, Phys. Rev. B **50**, 17953 (1994).

[29] G. Kresse and D. Joubert, From ultrasoft pseudopotentials to the projector augmented-wave method, Phys. Rev. B **59**, 1758 (1999).

[30] G. Kresse and J. Hafner, *Ab initio* molecular dynamics for liquid metals, Phys. Rev. B **47**, 558 (1993).

[31] G. Kresse and J. Furthmüller, Efficient iterative schemes for *ab initio* total-energy calculations using a plane-wave basis set, Phys. Rev. B **54**, 11169 (1996).

[32] J. P. Perdew, K. Burke, and M. Ernzerhof, Generalized Gradient Approximation Made Simple, Phys. Rev. Lett. **77**, 3865 (1996).

[33] Vladimir I. Anisimov, Jan Zaanen, and Ole K. Andersen, Band theory and mott insulators: Hubbard *U* instead of Stoner *I*, Phys. Rev. B **44**, 943 (1991).

[34] Carlo Adamo and Vincenzo Barone, Toward reliable density functional methods without adjustable parameters: The PBE0 model, J. Chem. Phys. **110**, 6158 (1999).

[35] Joachim Paier, Robin Hirschl, Martijn Marsman, and Georg Kresse, The Perdew-Burke-Ernzerhof exchange-correlation functional applied to the G2-1 test set using a plane-wave basis set, J. Chem. Phys. **122**, 234102 (2005).

[36] Bi-Ching Shih, Yubo Zhang, Wenqing Zhang, and Peihong Zhang, Screened Coulomb interaction of localized electrons in solids from first principles, Phys. Rev. B **85**, 045132 (2012).

[37] Stefano Baroni, Stefano de Gironcoli, Andrea Dal Corso, and Paolo Giannozzi, Phonons and related crystal properties from density-functional perturbation theory, Rev. Mod. Phys. **73**, 515 (2001).

[38] Rajesh Kumar, Neeraj Khare, Vijay Kumar, and G. L. Bhalla, Effect of intrinsic stress on the optical properties of nanostructured ZnO thin films grown by rf magnetron sputtering, Appl. Surf. Sci. **254**, 6509 (2008).

[39] S. Maniv, W. D. Westwood, and E. Colombini, Pressure and angle of incidence effects in reactive planar magnetron sputtered ZnO layers, J. Vac. Sci. Technol. **20**, 162 (1982).

[40] Margarita Baitimirova, Roman Viter, Jana Andzane, Arie van der Lee, Damien Voiry, Igor Iatsunskyi, Emerson Coy, Lina Mikoliunaite, Saulius Tumenas, Karol Załęski, Zigmas Balevicius, Ieva Baleviciute, Almira Ramanaviciene, Arunas Ramanavicius, Stefan Jurga, Donats Erts, and Mikhael Bechelany, Tuning of structural and optical properties of graphene/ZnO nanolaminates, J. Phys. Chem. C **120**, 23716 (2016).

[41] B. Meyer and Dominik Marx, Density-functional study of the structure and stability of ZnO surfaces, Phys. Rev. B **67**, 035403 (2003).

[42] Jamal Uddin and Gustavo E. Scuseria, Theoretical study of ZnO phases using a screened hybrid density functional, Phys. Rev. B **74**, 245115 (2006).

[43] R. Escudero and R. Escamilla, Ferromagnetic behavior of high-purity ZnO nanoparticles, Solid State Commun. **151**, 97 (2011).

[44] Robert Laskowski and Niels Egede Christensen, *Ab initio* calculation of excitons in ZnO, Phys. Rev. B **73**, 045201 (2006).

[45] C. L. Dong, C. Persson, L. Vayssieres, A. Augustsson, T. Schmitt, M. Mattesini, R. Ahuja, C. L. Chang, and J.-H. Guo, Electronic structure of nanostructured ZnO from x-ray absorption and emission spectroscopy and the local density approximation, Phys. Rev. B **70**, 195325 (2004).

[46] Walter R. L. Lambrecht, Anna V. Rodina, Sukit Limpijumnong, B. Segall, and Bruno K. Meyer, Valence-band ordering and magneto-optic exciton fine structure in ZnO, Phys. Rev. B **65**, 075207 (2002).

[47] Naoki Ohashi, Yutaka Adachi, Takeo Ohsawa, Kenji Matsumoto, Isao Sakaguchi, Hajime Haneda, Shigenori Ueda, Hideki Yoshikawa, and Keisuke Kobayashi, Polarity-dependent photoemission spectra of wurtzite-type zinc oxide, Appl. Phys. Lett. **94**, 122102 (2009).

[48] Elias Burstein, Anomalous optical absorption limit in InSb, Phys. Rev. **93**, 632 (1954).

[49] T. S. Moss, The interpretation of the properties of indium antimonide, Proc. Phys. Soc. London Sect. B **67**, 775 (1954).

[50] Aron Walsh, Juarez L. F. Da Silva, and Su-Huai Wei, Origins of band-gap renormalization in degenerately doped semiconductors, Phys. Rev. B **78**, 075211 (2008).